NANO LETTERS

Letter

pubs.acs.org/NanoLett

Pressure-Dependent Optical and Vibrational Properties of Monolayer Molybdenum Disulfide

Avinash P. Nayak,[†,▲] Tribhuwan Pandey,[‡,▲] Damien Voiry,[§] Jin Liu,[∥] Samuel T. Moran,[†] Ankit Sharma,[†] Cheng Tan,[†] Chang-Hsiao Chen,[¶] Lain-Jong Li,[○] Manish Chhowalla,[§] Jung-Fu Lin,[∥,⊥] Abhishek K. Singh,[*,‡] and Deji Akinwande[*,†]

[†]Department of Electrical and Computer Engineering, The University of Texas at Austin, Austin, Texas 78712, United States.

[‡]Materials Research Center, Indian Institute of Science, Bangalore 560-012, India

[§]Department of Materials Science and Engineering, Rutgers University, Piscataway Township, New Jersey 08854, United States

[∥]Department of Geological Sciences, The University of Texas at Austin, Austin, Texas 78712, United States

[⊥]Center for High Pressure Science and Technology Advanced Research (HPSTAR), Shanghai 201900, China

[¶]Institute of Atomic and Molecular Sciences, No. 1, Roosevelt Rd., Sec. 4, Taipei 10617, Taiwan

[○]Physical Science and Engineering Division, King Abdullah University of Science & Technology (KAUST), Thuwal 23955, Saudi Arabia

Supporting Information

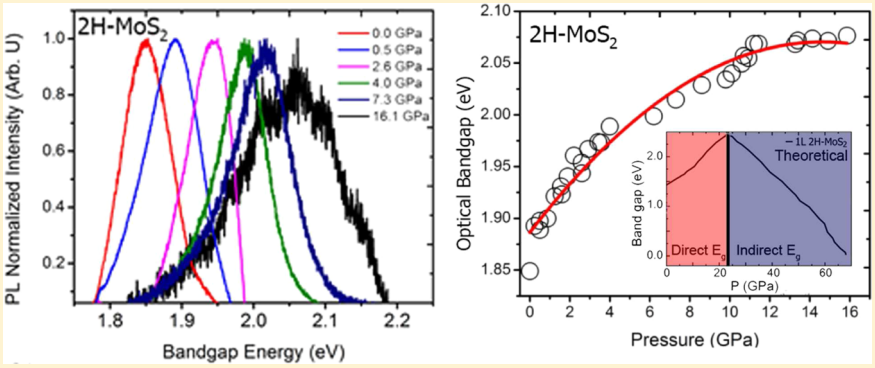

ABSTRACT: Controlling the band gap by tuning the lattice structure through pressure engineering is a relatively new route for tailoring the optoelectronic properties of two-dimensional (2D) materials. Here, we investigate the electronic structure and lattice vibrational dynamics of the distorted monolayer 1T-MoS_2 (1T′) and the monolayer 2H-MoS_2 via a diamond anvil cell (DAC) and density functional theory (DFT) calculations. The direct optical band gap of the monolayer 2H-MoS_2 increases by 11.7% from 1.85 to 2.08 eV, which is the highest reported for a 2D transition metal dichalcogenide (TMD) material. DFT calculations reveal a subsequent decrease in the band gap with eventual metallization of the monolayer 2H-MoS_2, an overall complex structure−property relation due to the rich band structure of MoS_2. Remarkably, the metastable 1T′-MoS_2 metallic state remains invariant with pressure, with the J_2, A_{1g}, and E_{2g} modes becoming dominant at high pressures. This substantial reversible tunability of the electronic and vibrational properties of the MoS_2 family can be extended to other 2D TMDs. These results present an important advance toward controlling the band structure and optoelectronic properties of monolayer MoS_2 via pressure, which has vital implications for enhanced device applications.

KEYWORDS: *2D Materials, MoS_2, Transition Metal Dichalcogenide, Strain, Hydrostatic Pressure, Diamond Anvil Cell, Pressure Engineering, Photoluminescence*

Among the great variety of exfoliable materials, transition metal dichalcogenides (TMD) have demonstrated promising optoelectronic properties. Interestingly, these properties can be largely tuned by varying the thickness,[1] by modifying the crystal structure,[2] or by applying strain on the TMDs.[3] Pressure engineering of the two-dimensional (2D) layered crystals is still a relatively new field with many possible routes for further investigations and optimization to fully realize their potential in materials engineering.[4−8] Being able to reversibly tune the band gap and structure of 2D materials by inducing pressure allows for exploring changes in photonic,[9] mechanical,[10] and electronic[11] properties at different hydrostatic pressures. The

Received: September 22, 2014
Revised: November 10, 2014

   dx.doi.org/10.1021/nl5036397 | *Nano Lett.* XXXX, XXX, XXX−XXX

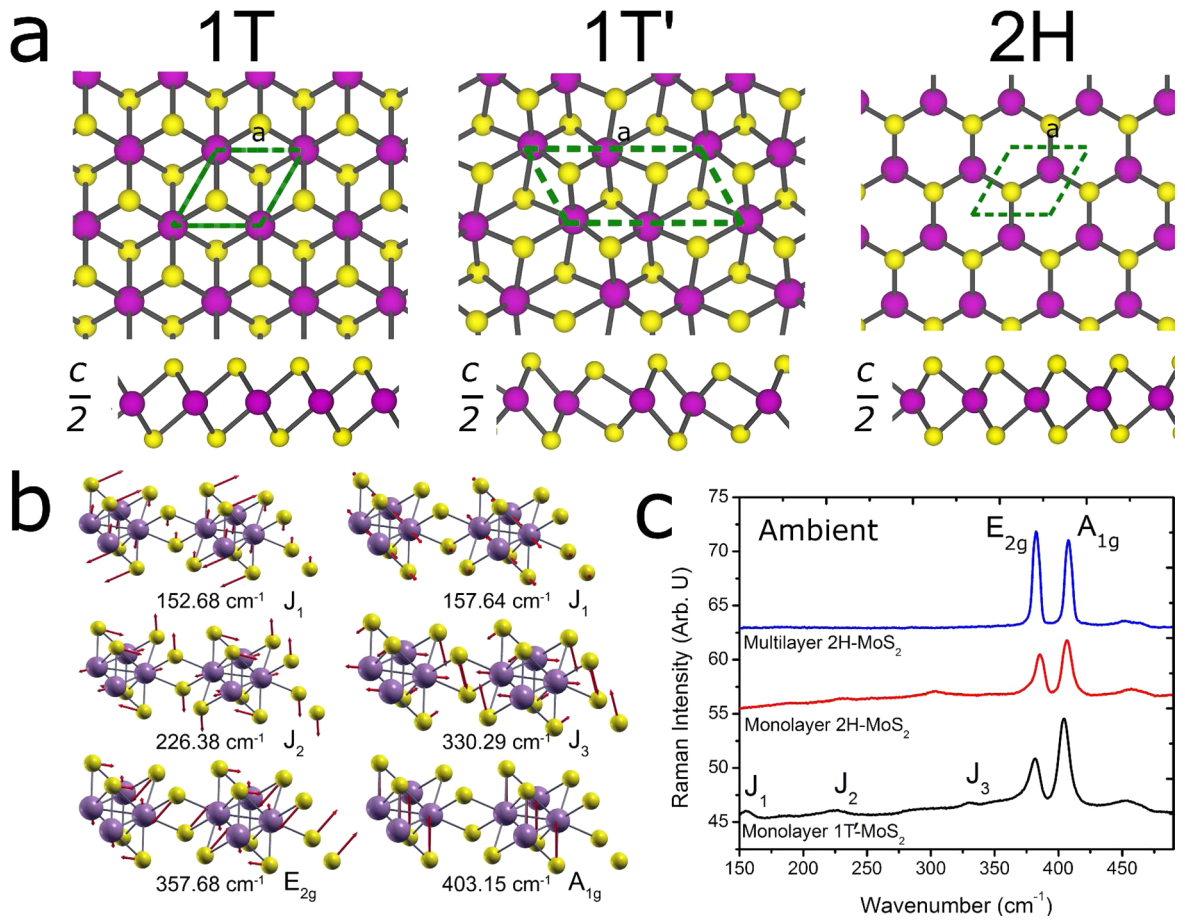

Figure 1. Structural and vibrational properties of monolayer MoS_2 polytypes. (a) Schematic atomic arrangements of the monolayer MoS_2 showing the *a* (in-plane direction) and the cross section *c* (out-of-plane) view of the monolayer 1T-MoS_2, 1T′-MoS_2, and 2H-MoS_2. (b) Raman active modes of the MoS_2 family. For the 1T′-MoS_2, the J_1 mode is composed of two Raman active modes that are close to one another and appear as one peak at room temperature. (c) Raman active modes for the restacked monolayer 1T′-MoS_2 and monolayer and bulk 2H-MoS_2. The J_1, J_2, and J_3 modes are only prominent in the 1T′-MoS_2 phase.

effects of hydrostatic pressure on 2D materials are important to understand, particularly for applications such as flexible electronics.[5]

The transition metal dichalcogenide family, which consists of 2D layered compounds, exhibits a laminar structure similar to that of graphene and has been investigated for several optoelectronic[1,12−14] and flexible[5,15] electronics. One representative TMD that has gained significant interest is molybdenum disulfide (MoS_2), which is composed of a single layer of Mo atoms covalently bonded between two laminar sheets of S atoms. The natural bulk 2H-MoS_2 is a semiconductor that has an indirect band gap of 1.3 eV, whereas its monolayer form has a direct band gap of 1.85 eV due to the lack of interlayer interactions in thinner layers.[1] Furthermore, depending on the arrangements of sulfur atoms in the lattice, Mo can be coordinated either by six sulfur atoms in an octahedral (1T), a distorted 1T (1T′), or a trigonal prismatic (2H) polytype[13] (Figure 1a). This different coordinated structure also changes the electronic structure of the material. The 1T′-MoS_2 is metallic, whereas the 2H-MoS_2 is semiconducting.

The two main Raman modes in the monolayer 2H-MoS_2 are the A_{1g} and the E_{2g} mode. The out-of-plane A_{1g} mode occurs due to opposing vibrations of the two S atoms with respect to the Mo atom. The E_{2g} mode is associated with the in-plane vibration of the Mo and S atoms, in opposite directions from one another. For the 1T′-MoS_2, the experimentally observed J_1 mode involves two different types of vibrations: one at 152.68 cm^{-1}, which is an out-of-plane motion of each stripe of the Mo atoms inside the zigzag chain, and the other mode at 157.64 cm^{-1}, which is an in-plane shearing vibration of one stripe of atoms with respect to the other atom in the chain. Both of these modes appear as a single peak at room temperature. The J_2 peaks at ∼226 cm^{-1} from the motion of two zigzag chains relative to each other, whereas the mode 330.29 cm^{-1}, named J_3, tends to break each zigzag chain in two stripes with a slight out-of-plane component (Figure 1b). Due to the atomic arrangements of the 1T′-MoS_2 and 2H-MoS_2 phases, these Raman modes with various magnitudes of activities can be used to decipher the lattice dynamics of the monolayer polytypes (Figure 1c).

It has been found experimentally that these two phases can transition to one another via interlayer atomic plane gliding, which displaces one of the S planes and changes its electronic state.[2,13,16] Another way to controllably alter the electronic properties is to mechanically distort the lattice structure by applying uniaxial, biaxial, or hydrostatic strain.[17−19] The majority of research in this field pertains to theoretical calculations on how the distortion of the 2H and 1T′-MoS_2 lattice can lead to changes in their photonic and electronic

dx.doi.org/10.1021/nl5036397 | *Nano Lett.* XXXX, XXX, XXX−XXX

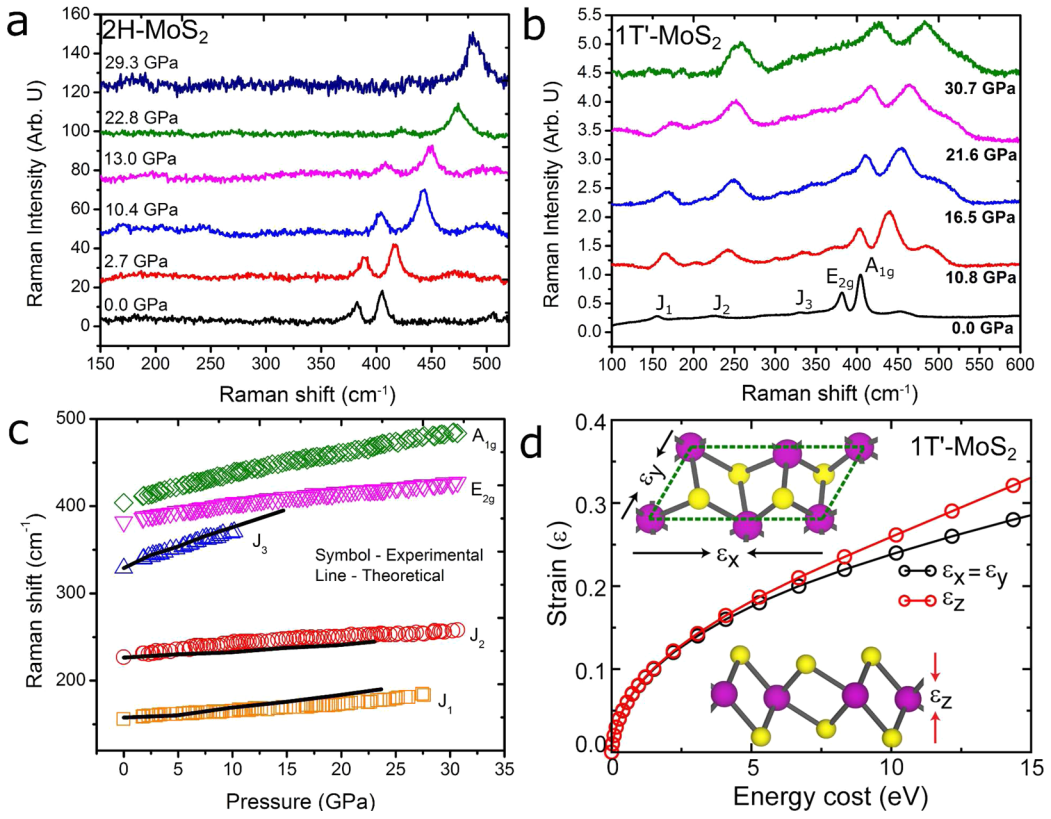

Figure 2. Pressure-dependent lattice vibrational properties of monolayer 1T′- and 2H-MoS_2. Representative Raman spectra of the monolayer (a) 2H-MoS_2 and (b) 1T′-MoS_2 at high pressures. For the 2H-MoS_2 polytype, the E_{2g} mode diminishes, whereas the dominant Raman modes are J_2, E_{2g}, and A_{1g} for 1T′-MoS_2 at pressures above 27 GPa. (c) Pressure-dependent Raman frequencies with variation in pressure for the five Raman active modes. The J_3 merges with the E_{2g} mode at around 10 GPa, whereas the J_1 diminishes at 27 GPa. The solid line indicates the theoretical agreement with the J_1, J_2, and J_3 modes and further supports the phonon merging of the J_3 and E_{2g} modes. (d) Applied strain is plotted with respect to the energy required to compress the in-plane and out-of-plane bonds, suggesting that the in-plane mode vibration is suppressed at higher pressures. Inset: Schematic representing the application of strain in the in-plane direction (ε_x, ε_y) (upper inset) and out-of-plane (ε_z) directions.

structure.[12,19−22] Experimentally, it has been a challenge to exert hydrostatic pressure homogeneously across a 2D sample, and only a nominal compressive strain of 0.2% or a uniaxial strain of 10% can be exerted with elaborate setups.[10,11]

In the present study, we have investigated the MoS_2 family (1T′-MoS_2 and both monolayer and bulk 2H-MoS_2) under extreme hydrostatic pressures up to 30 GPa. A diamond anvil cell (DAC) with a soft neon pressure medium was used to apply a hydrostatic pressure uniformly across the sample. The DAC experiments allow fundamental studies of the effects of high strain levels on the properties of materials, MoS_2 in this case. This sort of study is important for probing the intrinsic response of the strain-property relations in a controlled environment. The insights provided by this study can guide practical realization of strained MoS_2 devices. The DAC methodology also permits us to investigate the modulation of the band gap, the shift from a direct to an indirect band gap, and the altered phononic properties of both the monolayer 2H-MoS_2 and 1T′-MoS_2 under applied hydrostatic pressures. These results show that for the monolayer 2H-MoS_2 polytype a ∼12% increase in band gap is observed. Although a higher pressure is not experimentally achievable for the time being, a metallization at 68 GPa is predicted by theoretical calculations. The semiconductor to metal transition occurs at a much higher pressure than that in the bulk counterpart which metalizes at ∼19 GPa. For the 1T′-MoS_2 polytype, the out-of-plane vibrations are hindered by the hydrostatic pressure, allowing only the J_2, A_{1g}, and E_{2g} vibrational modes to become dominant at pressures past 27 GPa. Our combined experimental and theoretical results allow for a coherent understanding of the vibrational, optical, and electronic properties of TMD materials as a function of the number of layers and layer geometry under hydrostatic pressure.

Raman spectroscopy, being fast and nondestructive, is a powerful diagnostic tool to investigate the vibrational and physical properties of MoS_2. Raman spectroscopy has been used to study 2H-MoS_2 to determine the number of layers,[23] to determine the effect of pressure on the 2H-MoS_2 lattice,[24−26] and to determine the level of doping[27] and defects.[28,29] To understand the electronic and mechanical stability of the MoS_2 polytypes, we have studied the monolayer and bulk 2H-MoS_2 as well as restacked monolayer 1T′-MoS_2 under hydrostatic pressure.

The lattice vibrations detected by Raman spectroscopy can reveal key changes occurring to the lattice at high pressures. In particular, hydrostatic pressure can induce a blue shift (phonon hardening) in MoS_2.[17] For the 2H-MoS_2 monolayer polytype, the intensity of in-plane Raman mode (E_{2g}) starts to diminish at pressures above 16 GPa (Figure 2a). The intensity ratio of A_{1g}/E_{2g} also increases with pressure (Supporting Information Figure S1a) above 16 GPa. The diminishing intensity of the E_{2g} mode is attributed to the dominance of normal compressive strain on the monolayer 2H-MoS_2 under large hydrostatic pressures,[30] which hinders the in-plane E_{2g} movement, whereas

dx.doi.org/10.1021/nl5036397 | Nano Lett. XXXX, XXX, XXX−XXX

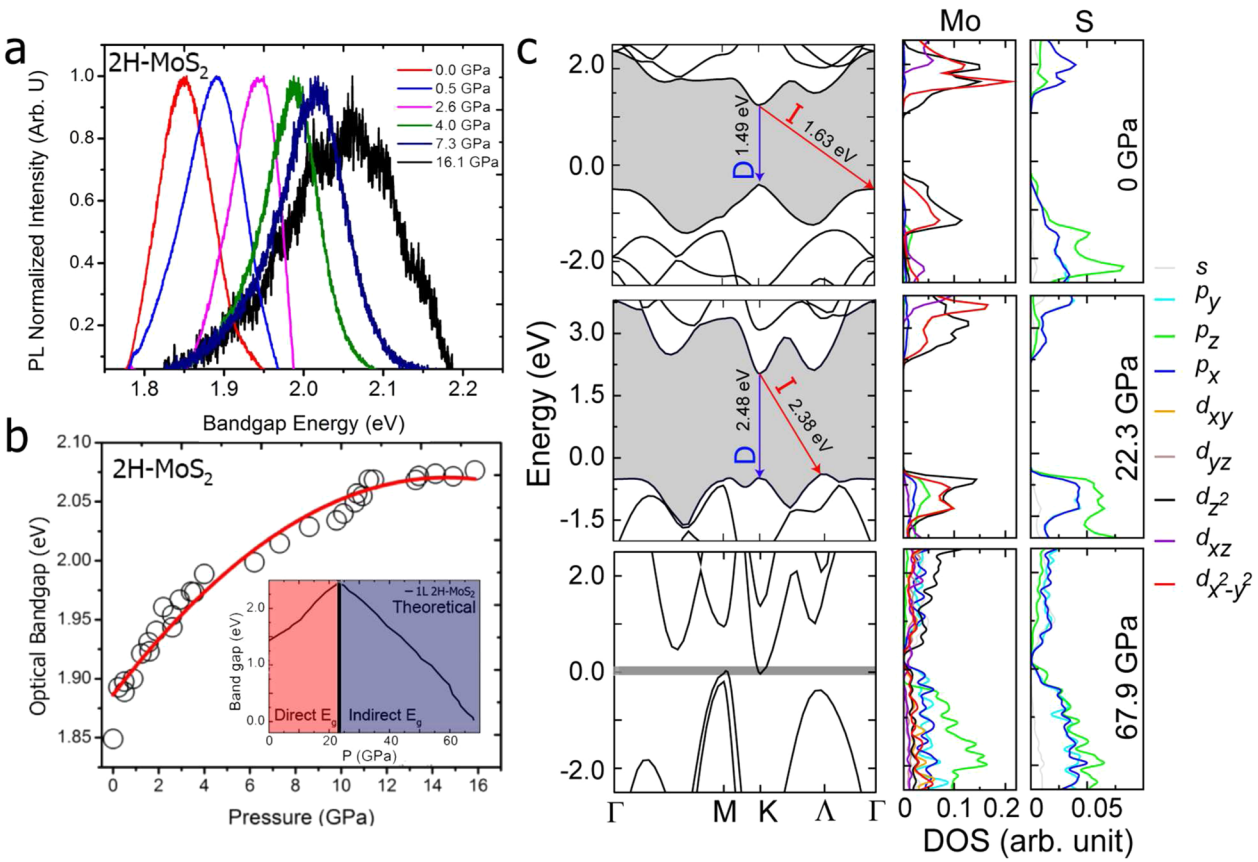

Figure 3. Pressure modulated photoluminescent properties of monolayer 2H-MoS_2. (a) Representative PL spectra as a function of pressure. An increase in the band gap with increasing pressure and then the diminishing of the PL signals at ∼16 GPa indicates a direct-to-indirect band gap shift. (b) Derived band gap at high pressures. Extracted from the Lorentzian fit from the PL peaks, the band gap is shown to increase as a function of pressure. Red solid line: a polynomial fit to the experimental data described by $E_g = 1.88 + 0.03P - 8.59 \times 10^{-4}P^2$ where E_g is optical band gap and P is pressure. Inset: The theoretical prediction of the direct-to indirect band gap transition. (c) Band gap diagrams at M, K, Λ, and Γ point at two representative pressures of 0 and 22.3 GPa depicting the direct to indirect transition. Here, D and I indicate the direct and indirect band gaps, respectively. The observed direct and indirect band gap values are also presented for clarity. At 0 GPa, the $E-k$ diagram indicates a direct-band gap between the CBM and the VBM, whereas at 22.3 GPa, band gap shift form direct (from in between K−K′ points) to indirect in between K−Λ points at 22.6 GPa that agrees with the experimental observations. At around 67.9 GPa the valence band maxima (VBM) and the conduction band minima (CBM) cross the Fermi level, leading to a semiconductor-to-metal transition.

the A_{1g} out-of-plane vibrational mode is still prominent at pressures up to 30 GPa.

Although the rate of increase is higher for A_{1g} mode (Supporting Information Figure S1b), the E_{2g} mode also increases linearly. This distinct rate of increase can be explained by analyzing the type of vibrations involved in A_{1g} and E_{2g} modes. The A_{1g} modes originate from transverse vibrations of the S−S atom; however, the E_{2g} mode emerges from longitudinal vibrations of Mo and S atoms in opposite directions. The change in Mo−S bond length (in-plane movement of atoms) plays a significant role in determining the behavior of the E_{2g} mode. As the hydrostatic pressure increases, the out-of-plane (A_{1g}) compression becomes more favorable than the in-plane (E_{2g}) compression, indicating that at higher pressures, the transverse moment of the S−S atom is faster than the in-plane movement of the Mo−S atom (Supporting Information Figure S2a). This results in a higher rate of increase of A_{1g} mode with increasing pressure in comparison to E_{2g} mode.

Although several studies have been done on the synthesis and characterization[13,31] of the distorted octahedral 1T′-MoS_2 polytype, the lattice vibrations at extreme hydrostatic pressure conditions have not yet been studied. Previous theoretical studies have shown the breaking of lattice symmetry in 1T′-MoS_2 when tensile and compressive strain are applied.[20] The 1T′-MoS_2 phase shows three Raman active modes that are not present in the trigonal prismatic 2H-MoS_2 polytype. These three extra modes are the J_1, J_2, and J_3, which show up at 150 cm^{-1}, 225 cm^{-1}, and 325 cm^{-1}, respectively, at ambient pressure. As the hydrostatic pressure increases, J_3 becomes indistinguishable from the E_{2g} mode at ∼10 GPa, whereas J_1 and J_2 are still prominent at higher pressures. The broadening of the J_3 mode with pressure further supports the merging phenomenon of the J_3 and E_{2g} modes (Supporting Information Figure S3). In order to confirm this phonon merging, theoretical calculations have been carried out to investigate the effect of pressure on the vibrational properties of the monolayer 1T′-MoS_2. The calculated phonon dispersion curves (Supporting Information Figure S4) at ambient pressure are consistent with the previously reported results[32] and were used to identify all the Raman active modes. The theoretically derived pressure-dependent Raman frequencies show good qualitative agreement with experimental observation. The Raman intensity increases for the J_1, A_{1g}, and E_{2g} modes and shows the merging of the J_3 and E_{2g} modes (Supporting Information Figure S5). The J_1 Raman mode also diminishes at

dx.doi.org/10.1021/nl5036397 | Nano Lett. XXXX, XXX, XXX−XXX

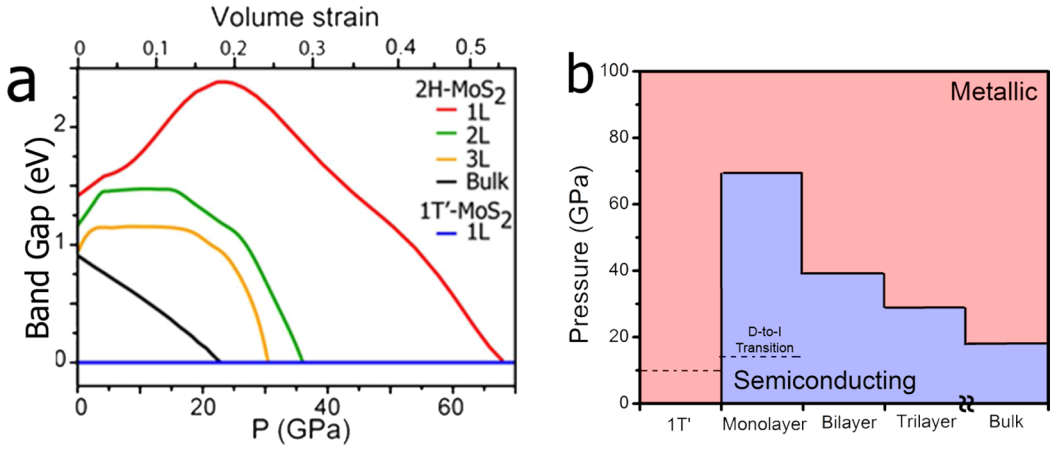

Figure 4. Electronic structures of the MoS_2 polytypes under hydrostatic pressure. (a) Band gap energies of the polytypes as a function of pressure. (a) Below 22.3 GPa, an increase in the direct band gap is observed for the monolayer 2H-MoS_2, whereas for higher pressure, the band gap decreases with strain and closes at 67.9 GPa indicating a metallization transition. A smaller critical pressure of 39.2 and 29.5 GPa is observed for the bilayer and trilayer 2H-MoS_2 respectively. (b) Hydrostatic pressure effects on monolayer, bilayer, trilayer, bulk MoS_2, and 1T′-MoS_2. A metallic state is more easily reached in the bulk state because more interlayer interactions are present.

pressures above 22 GPa, leaving just the J_2, the A_{1g}, and the E_{2g} Raman modes dominant at pressures past 27 GPa (Figure 2b). To investigate the E_{2g} and J_3 merging in further detail, theoretical calculations were performed to find the dependence on pressure compared to the other modes (Figure 2c). As the hydrostatic pressure increases, the out-of-plane compression becomes more favorable (0.08 Å/GPa) than the in-plane compression (0.03 Å/GPa), suggesting that at higher pressures the out-of-plane moment of the S−S atom is faster than the Mo−S movement leading to a smaller rate of increase of the E_{2g} mode (1.3 cm^{-1}/GPa) compared to the A_{1g} mode (2.5 cm^{-1}/GPa) (Figure 2d). The pressure-dependent rate of increase for the J_1 and J_2 Raman mode is 0.9 cm^{-1}/GPa, whereas the J_3 mode increases at 3.90 cm^{-1}/GPa. For the 2H-MoS_2 polytype, the pressure dependence on the Raman modes of the monolayer 2H-MoS_2, 1T′-MoS_2 and the bulk 2H-MoS_2 show that the A_{1g} and E_{2g} modes for both the monolayer 2H-MoS_2 and 1T′-MoS_2 polytypes are similar (Supporting Information Figure S6). For the 2H-MoS_2 monolayer, the shift in Raman peak position increases linearly with applied pressure. The Raman shift with pressure for the A_{1g} mode is 2.6 cm^{-1}/GPa, whereas the E_{2g} mode increases at a rate of 1.7 cm^{-1}/GPa (Supporting Information Figure S1b). The distance between A_{1g} and E_{2g} Raman modes increases at a rate of 1.2 cm^{-1}/GPa (Supporting Information Figure S1c). The A_{1g} shift for monolayer MoS_2 with pressure, in comparison with other 2D materials such as $MoSe_2$, $MoTe_2$, and ReS_2, is higher, signifying that the monolayer MoS_2 has a strong dependence on pressure.[33] The deviation from the bulk MoS_2 is mainly attributed to the interlayer interactions along the out-of-plane axis, which is absent in the monolayer. Unlike the bulk 2H-MoS_2, no intermediate phase region between the semiconducting and metallic region is observed, indicating that the monolayer MoS_2 does not undergo metallization or a structural transition at pressures up to 30 GPa. Theoretically, we predict the metallization of 2H-MoS_2 to be at ∼68 GPa.

Due to the inherent direct band gap (1.85 eV) of the monolayer 2H-MoS_2, the photonic and electronic band structure can be probed by photoluminescence (PL) spectroscopy.[29] This strong PL emission is only observed in the monolayer 2H-MoS_2 and is attributed to the slow electronic relaxation that is unique to its electronic structure. The PL signal for the bilayer and trilayer are much weaker.[29] Our PL spectral measurements on the monolayer 2H-MoS_2 show that the electronic band structure can be significantly modulated by hydrostatic pressure (Figure 3a) at a rate of 30 meV/GPa below 5 GPa. At higher pressures, the direct band gap gradually increases to 2.08 eV at ∼12 GPa, showing a significant 11.7% change in band gap (Figure 3b), while increasing the PL full width half-maximum (fwhm) (Supporting Information Figure S1d). Although this increase in the direct band gap is reversible (Supporting Information Figure S7), the rate of increase can be altered depending on the pressure medium. This can significantly modify the photonic and electronic characteristics of 2D materials under high pressure.[6,9,34] Because we have used an inert, soft Ne pressure medium in our experiments, our results therefore represent more intrinsic features of the system without dopant effects. The polynomial increase in the band energy is in agreement with theoretical DFT calculations, which show an increase in the direct band gap at the K−K′ point. The theoretical band gap is underestimated due to the presence of artificial self-interaction and the absence of the derivative discontinuity in the exchange-correlation potential with the PBE/GGA methods.[35] The initial trend in band gap as supported by the PL experiments (Figure 3b) shows an increase at the K−K′ point. The in situ fwhm map of PL Spectra (Supporting Information Figure S8) increases from 24.7 nm at 0.6 GPa to 58.7 nm at 12.5 GPa and diminishes to the background noise level at pressures over 16 GPa at room temperature. This increase in the fwhm implies a crossover point to the direct-to-indirect band gap[3] at the K−K′ point at approximately 16 GPa. This direct to indirect band gap shift was further conformed by DFT calculations. The ambient theoretical band gap initially lies in-between K−K′ point until a pressure of 22.3 GPa is reached. At 22.3 GPa, a direct-to-indirect transition indicates that the conduction band minima (CBM) and the valence band maxima (VBM) are no longer at the K−K′ interband (Figure 3c), but rather shift to the K−Λ point. Theoretical calculations reveal that the band gap of 2H-MoS_2 monolayer first increases until a pressure of ∼22 GPa is reached. Beyond this pressure, the band gap gradually

dx.doi.org/10.1021/nl5036397 | Nano Lett. XXXX, XXX, XXX−XXX

decreases, eventually leading to the metallization of monolayer 2H-MoS_2 at around 68 GPa.

To understand the mechanism for this band gap change and the semiconductor to metal (S−M) transition under hydrostatic pressure, we analyze the contribution from different molecular orbitals by performing angular momentum projected density of states (LDOS) calculations. At lower pressures, both valence (VB) and conduction bands (CB) are mainly composed of Mo-$d_{x^2-y^2}$, d_{z^2} and S-p_x, p_y orbitals (Figure 3c). With increasing pressure, these orbitals move away from the Fermi level, resulting in an increase in band gap up to 22.3 GPa pressure. At higher pressure, the out-of-plane compression becomes more dominant (Supporting Information Figure S2b), which makes the Mo d_{z^2}, d_{xz}, and p_z orbitals interact strongly with S p_z and p_x orbitals. This strong intralayer hybridization between the orbitals mentioned above leads to a decrease in band gap after ∼22 GPa pressure and finally closing of the band gap at higher pressure (68 GPa). For the monolayer 2H-MoS_2, in-plane intralayer interactions play a dominant role in the metallization at 67.9 GPa.

It was found in our previous study of the bulk MoS_2 that interlayer interactions play a critical role in the metallization.[17] It is therefore expected that as the number of layers increases, the critical pressure or critical volume strain (Supporting Information Figure S10) at which the metallization occurs decreases (Figure 4a). The metallization of the bilayer, trilayer, and bulk 1T′-MoS_2 (Figure 4a and b) under high pressure can be understood by the interaction of electron-donating sulfur atoms between the van der Waals gaps.[17,21] The transition pressure for MoS_2 therefore decreases as the number of layers increases. As experimentally observed, the monolayer 1T′-MoS_2 shows metallic behavior (Supporting Information Figure S7), unlike the 2H-MoS_2 polytype which is semiconducting in nature. For the 2H-MoS_2, the valence and conduction bands are mainly composed of the *d* orbitals of Mo and *p* orbitals of S atoms (Supporting Information Figure S11a). Upon application of hydrostatic pressure the extent of hybridization between Mo *d* orbitals (mainly d_{z^2}, d_{xy}, and $d_{x^2-y^2}$) and S *p* orbitals increases, thus increasing the overlap between conduction and valence bands resulting in an enhanced metallization (Supporting Information Figure S11b).

We have measured an 11.7% in the direct band gap of the 2H-MoS_2 from 1.85 eV at ambient pressure to 2.08 eV at 16 GPa before the PL signal diminished and could no longer be resolved at higher pressures and room temperature. For comparison, a 3.3% difference in direct band gap was found by S.P. Lau et al.,[11] a 3.0% difference by G. A. Steele et al.,[36] and a 5.4% difference by Dou et al.[9] for the monolayer 2H-MoS_2. To further understand the electronic and phononic properties, DFT calculations were conducted to show that a critical pressure of 67.9 GPa is required to metalize the monolayer 2H-MoS_2. The 1T′-MoS_2 behaves as a metal at ambient pressure and exhibits three more Raman active modes (J_1, J_2, and J_3) in comparison to the 2H-MoS_2, which exhibits just the A_{1g} and E_{2g} modes. At pressures above 10 and 27 GPa, we have observed the diminishing of the out-of-plane J_1 and J_3 Raman modes, respectively, due to higher susceptibility to hydrostatic pressure along the out-of-plane axis. At 10 GPa, the J_3 mode starts to merge with the E_{2g} mode. The suppression of the J_1 mode at ∼27 GPa is attributed to the large hydrostatic pressure on the lattice implying that the effect of pressure is more pronounced for this mode and is more sensitive to pressure. Because this process is reversible for both the 2H-MoS_2 and the 1T′-MoS_2, the distortion of the lattice is predicted to be a transitory structural modification. The total energy calculation also reveals that monolayer MoS_2 is the most stable phase under the applied pressure range (Supporting Information Figure S12), and confirms that there is no phase transformation between 2H and 1T′ phase within the studied range of pressure.

Strain engineering of 2D layered materials is a relatively new field with possible routes for further investigations to fully realize their potential in customizing material behavior. Here, the interplay of the structural and optoelectronic properties is successfully described for the MoS_2 family. The monolayer 2H-MoS_2 differs from its bulk counterpart because the bandgap increases by ∼12% with applied hydrostatic pressure due to the absence of interlayer interactions. For the intrinsically metallic 1T′-MoS_2, interlayer structural distortion is prevalent resulting in phonon merging of two Raman active modes (J_1 and E_{2g}) at high pressures. The large reversible bandgap modulation of semiconducting MoS_2 is attractive for highly tunable optoelectronics, nanoelectronics, and flexible electronics and can enable new opportunities based on the dynamic strong electron−phonon coupling.

Experimental Methods. *Sample Preparation.* The 2H-MoS_2 monolayer was synthesized based on our previous work.[37] In brief, 300 nm SiO_2 substrates were placed in the center of a tubular furnace. Precursors of 0.3 g MoO_3 (Sigma-Aldrich, 99.5%) in Al_2O_3 crucible was placed 12 cm away from substrates and S (Sigma-Aldrich, 99.5%) powder in quartz tube was evaporated in tube and reacted with Al_2O_3. The furnace was first heated to 150 °C at 10 °C/min rate with 70 sccm Ar at 10 Torr and annealed for 20 min, then reached 650 °C at 25 °C/min rate and kept for 1 h. After growth, furnace was slowly cooled to room temperature. The as-grown MoS_2 film was broken into thin pieces that were used after cleaning the substrate with acetone. The thinned down sample was transferred over to the DAC by a 10 μm edged tweezer and was studied as is.

1T′-MoS_2 samples were synthesized by Li intercalation using *n*-butyllithium as explained elsewhere.[13] The Li_xMoS_2 was retrieved by filtration and washed with hexane (60 mL) to remove excess *n*-butyllithium and other organic residues. Exfoliation was achieved by ultrasonicating Li_xMoS_2 in water at a concentration of 1 mg/mL for 1 h. The mixture was centrifuged several times to remove lithium cations in the form of LiOH as well as nonexfoliated materials.

Characterization. For the Raman spectroscopic studies on the 2H and 1T′ polytypes, a green 532 nm Coherent Verdi V2 laser was used at the Mineral Physics Laboratory of the University of Texas at Austin. The scattered light was dispersed by a 1800 grooves/mm grating and collected by an EMCCD (Andor Technology) resulting in a spectral resolution of approximately 1 cm^{-1}. To avoid potential overheating or oxidizing of the samples, the highest laser power level used was 20 mW with a focused laser beam size of 10 μm. Ruby fluorescence spectra were also collected using the same system for pressure calibrations[38] (Supporting Information Figure S8).

For the photoluminescence (PL) and Raman in situ mapping studies on the 2H-MoS_2, a grating of 900 grooves/mm was used. A long working-distance (LD EC) objective, Epiplan-Neofluar (20*x*/0.22 DIC M27), was used. The Witec Alpha 300 micro-Raman confocal microscope with a 488 nm laser was used for the in situ PL and Raman mapping studies. To better understand the band gap energy of the system, a Lorentzian

dx.doi.org/10.1021/nl5036397 | *Nano Lett.* XXXX, XXX, XXX−XXX

curve fit to the PL curves was used to derive the peak energy positions as well as the band widths.[39]

Theoretical Calculations. *Modeling of Hydrostatic Pressure on Monolayer MoS_2.* The hydrostatic pressure on the monolayer was modeled by calculating the ease of compression along the *x*, *y*, and *z* direction. First, we checked the individual energy costs for in-plane (*x*, *y*) and out of plane compression (*z*). Based on the energy cost calculation we calculated the compression along all directions for hydrostatic pressure modeling (Supporting Information Figure S2a and S2b). A similar procedure was followed for 1T′- MoS_2 monolayer.

For 2L, 3L, and bulk MoS_2, first we approximate the in-plane (change in *a*, *b*) and out-of-plane (change in slab thickness *c*) compression by performing total energy calculation. First, we apply a uniform strain in all directions calculate the energy cost. By comparing the energy cost for biaxial and normal compressive strain, we extract the atomic displacement. Due to presence of weak van der Waals (vdW) interaction in between the layers the slab thickens decreases more rapidly in comparison to in plane lattice parameter *a* and *b* as shown in Supporting Information Figure S13 (a) for 2L MoS_2.

In order to correlate the theoretical finding with experiments, it is important to estimate applied hydrostatic pressure. The applied pressure was calculated from the energy cost per unit volume as per the following equation for 1L, 2L, 3L, and bulk MoS_2

$$P = \frac{E - E_0}{V - V_0}$$

where, E (E_0) and V (V_0) are the energy and volume for the unstrained (strained) systems. The volume of a hexagonal lattice can be defined as $V = a^2\, c\, sin\,(60)$ where *a* is the in-plane lattice parameter and *c* is thickness of slab. The thickness of various structures is defined as shown in Supporting Information Figure S13. As shown in our previous work,[17] the theoretical calculated pressure agrees well with the experimental pressure for bulk MoS_2.

First-Principles Theoretical Calculations. Theoretical calculations were performed using first-principle ab initio density functional theory (DFT) using Vienna Ab Initio Simulation Package (VASP).[40] All-electron projector augmented wave potentials[41,42] and the Perdew−Burke−Ernzerhof[43] generalized gradient approximation (GGA) were used to account for the electronic exchange and correlation. The structure of the 1T′-MoS_2 monolayer is generated by following the approach of Calandra.[23] All the structures were relaxed in the *x*−*y* plane while constraining the *z* coordinates by employing a conjugate gradient scheme until the forces on every atom were minimized to be less than 0.005 eV/Å. A well-converged Monkhorst−Pack **k** point set of 15 × 15 × 1 was used for this procedure. The phonon dispersion of monolayer MoS_2 was calculated using density functional perturbation theory (DFPT)[44] as implemented in VASP. An additional tool, Phonopy,[45] which supports the VASP interface, was used for extracting the phonon frequencies. The force constants were calculated with a supercell of 2 × 2 × 1 and the **k** point set of 13 × 13 × 1. In order to obtain accurate phonon frequencies, a high energy cutoff of 600 eV and strict energy convergence criterion of 10^{-11} eV were used.

■ ASSOCIATED CONTENT

Ⓢ Supporting Information

Here, you will find further experimental and theoretical support for the optical and structural properties discussed in this manuscript. This material is available free of charge via the Internet at http://pubs.acs.org.

■ AUTHOR INFORMATION

Corresponding Authors

*E-mail: deji@ece.utexas.edu.

*E-mail: abhishek@mrc.iisc.ernet.in.

Author Contributions

▲The manuscript was written through contributions of all authors. All authors have given approval to the final version of the manuscript. These authors contributed equally.

Notes

The authors declare no competing financial interest.

■ ACKNOWLEDGMENTS

Research at The University of Texas at Austin was supported in by a Young Investigator Award (D.A.) from the Defense Threat Reduction Agency (DTRA), the Army Research Office (ARO), and the Southwest Academy of Nanoelectronics (SWAN) center sponsored by the Semiconductor Research Corporation (SRC). Research at Indian Institute of Science was supported by National Program on Micro and Smart Systems (NpMASS) PARC No. 1:22 and DST Nanomission. We would like to thank Megan Matheney for providing critical feedback. J.F.L. acknowledges supports from Energy Frontier Research in Extreme Environments (EFree), Center for High Pressure Science and Advanced Technology (HPSTAR), and the U.S. National Science Foundation Geophysics Program. L.J.L. acknowledges support from Academia Sinica Taiwan and KAUST, Saudi Arabia.

■ REFERENCES

(1) Mak, K. F.; Lee, C.; Hone, J.; Shan, J.; Heinz, T. F. *Phys. Rev. Lett.* **2010**, *105* (13), 136805.

(2) Chhowalla, M.; Shin, H. S.; Eda, G.; Li, L.-J.; Loh, K. P.; Zhang, H. *Nat. Chem.* **2013**, *5* (4), 263−275.

(3) Conley, H. J.; Wang, B.; Ziegler, J. I.; Haglund, R. F.; Pantelides, S. T.; Bolotin, K. I. *Nano Lett.* **2013**, *13* (8), 3626−3630.

(4) Artyukhov, V. I.; Liu, M.; Yakobson, B. I. *Nano Lett.* **2014**, *14* (8), 4224−4229.

(5) Chang, H.-Y.; Yang, S.; Lee, J.; Tao, L.; Hwang, W.-S.; Jena, D.; Lu, N.; Akinwande, D. *ACS Nano* **2013**, *7* (6), 5446−5452.

(6) Proctor, J. E.; Gregoryanz, E.; Novoselov, K. S.; Lotya, M.; Coleman, J. N.; Halsall, M. P. *Phys. Rev. B* **2009**, *80* (7), 073408.

(7) Restrepo, O. D.; Mishra, R.; Goldberger, J. E.; Windl, W. *J. Appl. Phys.* **2014**, *115* (3), 033711−033711−8.

(8) Frank, O.; Tsoukleri, G.; Riaz, I.; Papagelis, K.; Parthenios, J.; Ferrari, A. C.; Geim, A. K.; Novoselov, K. S.; Galiotis, C. *Nat. Commun.* **2011**, *2*, 255.

(9) Dou, X.; Ding, K.; Jiang, D.; Sun, B. *ACS Nano* **2014**, *8* (7), 7458−7464.

(10) Pérez Garza, H. H.; Kievit, E. W.; Schneider, G. F.; Staufer, U. *Nano Lett.* **2014**, *14* (7), 4107−4113.

(11) Hui, Y. Y.; Liu, X.; Jie, W.; Chan, N. Y.; Hao, J.; Hsu, Y.-T.; Li, L.-J.; Guo, W.; Lau, S. P. *ACS Nano* **2013**, *7* (8), 7126−7131.

(12) Najmaei, S.; Zou, X.; Er, D.; Li, J.; Jin, Z.; Gao, W.; Zhang, Q.; Park, S.; Ge, L.; Lei, S.; Kono, J.; Shenoy, V. B.; Yakobson, B. I.; George, A.; Ajayan, P. M.; Lou, J. *Nano Lett.* **2014**, *14* (3), 1354−1361.

(13) Eda, G.; Yamaguchi, H.; Voiry, D.; Fujita, T.; Chen, M.; Chhowalla, M. *Nano Lett.* **2011**, *11* (12), 5111−5116.

(14) Ganatra, R.; Zhang, Q. *ACS Nano* **2014**, *8* (5), 4074−4099.
(15) Lee, J.; Tao, L.; Parrish, K. N.; Hao, Y.; Ruoff, R. S.; Akinwande, D. *Appl. Phys. Lett.* **2012**, *101* (25), 252109−2−252109−4.
(16) Duerloo, K.-A. N.; Li, Y.; Reed, E. J. *Nat. Commun.* **2014**, *5*, 1−9.
(17) Nayak, A. P.; Bhattacharyya, S.; Zhu, J.; Liu, J.; Wu, X.; Pandey, T.; Jin, C.; Singh, A. K.; Akinwande, D.; Lin, J.-F. *Nat. Commun.* **2014**, *5*, 1−9.
(18) Bissett, M. A.; Tsuji, M.; Ago, H. *Phys. Chem. Chem. Phys.* **2014**, *16* (23), 11124−11138.
(19) Guo, H.; Lu, N.; Wang, L.; Wu, X.; Zeng, X. C. *J. Phys. Chem. C* **2014**, *118* (13), 7242−7249.
(20) Hu, T.; Li, R.; Dong, J. *J. Chem. Phys.* **2013**, *139* (17), 1747022−1747027.
(21) Bhattacharyya, S.; Singh, A. K. *Phys. Rev. B* **2012**, *86* (7), 075454.
(22) Espejo, C.; Rangel, T.; Romero, A. H.; Gonze, X.; Rignanese, G. M. *Phys. Rev. B* **2013**, *87* (24), 245114.
(23) Terrones, H.; Corro, E. D.; Feng, S.; Poumirol, J. M.; Rhodes, D.; Smirnov, D.; Pradhan, N. R.; Lin, Z.; Nguyen, M. A. T.; Elias, A. L.; Mallouk, T. E.; Balicas, L.; Pimenta, M. A.; Terrones, M. *Sci. Rep.* **2014**, *4*, 1−9.
(24) Sugai, S.; Ueda, T. *Phys. Rev. B* **1982**, *26* (12), 6554−6558.
(25) Aksoy, R.; Selvi, E.; Ma, Y. *J. Phys. Chem. Solids* **2008**, *69* (9), 2138−2140.
(26) Chi, Z.-H.; Zhao, X.-M.; Zhang, H.; Goncharov, A. F.; Lobanov, S. S.; Kagayama, T.; Sakata, M.; Chen, X.-J. *Phys. Rev. Lett.* **2014**, *113* (3), 036802.
(27) Sercombe, D.; Schwarz, S.; Pozo-Zamudio, O. D.; Liu, F.; Robinson, B. J.; Chekhovich, E. A.; Tartakovskii, I. I.; Kolosov, O.; Tartakovskii, A. I. *Sci. Rep.* **2013**, *3*, 1−6.
(28) Ling, X.; Fang, W.; Lee, Y.-H.; Araujo, P. T.; Zhang, X.; Rodriguez-Nieva, J. F.; Lin, Y.; Zhang, J.; Kong, J.; Dresselhaus, M. S. *Nano Lett.* **2014**, *14* (6), 3033−3040.
(29) Li, H.; Zhang, Q.; Yap, C. C. R.; Tay, B. K.; Edwin, T. H. T.; Olivier, A.; Baillargeat, D. *Adv. Funct. Mater.* **2012**, *22* (7), 1385−1390.
(30) Bandaru, N.; Kumar, R. S.; Sneed, D.; Tschauner, O.; Baker, J.; Antonio, D.; Luo, S.-N.; Hartmann, T.; Zhao, Y.; Venkat, R. *J. Phys. Chem. C* **2014**, *118* (6), 3230−3235.
(31) Jiménez Sandoval, S.; Yang, D.; Frindt, R. F.; Irwin, J. C. *Phys. Rev. B* **1991**, *44* (8), 3955−3962.
(32) Calandra, M. *Phys. Rev. B* **2013**, *88* (24), 245428.
(33) Tongay, S.; Sahin, H.; Ko, C.; Luce, A.; Fan, W.; Liu, K.; Zhou, J.; Huang, Y.-S.; Ho, C.-H.; Yan, J.; Ogletree, D. F.; Aloni, S.; Ji, J.; Li, S.; Li, J.; Peeters, F. M.; Wu, J. *Nat. Commun.* **2014**, *5*, 1−6.
(34) Nicolle, J.; Machon, D.; Poncharal, P.; Pierre-Louis, O.; San-Miguel, A. *Nano Lett.* **2011**, *11* (9), 3564−3568.
(35) Perdew, J. P.; Zunger, A. *Phys. Rev. B* **1981**, *23* (10), 5048−5079.
(36) Castellanos-Gomez, A.; Roldán, R.; Cappelluti, E.; Buscema, M.; Guinea, F.; van der Zant, H. S. J.; Steele, G. A. *Nano Lett.* **2013**, *13* (11), 5361−5366.
(37) Lee, Y.-H.; Zhang, X.-Q.; Zhang, W.; Chang, M.-T.; Lin, C.-T.; Chang, K.-D.; Yu, Y.-C.; Wang, J. T.-W.; Chang, C.-S.; Li, L.-J.; Lin, T.-W. *Adv. Mater.* **2012**, *24* (17), 2320−2325.
(38) Mao, H. K.; Xu, J.; Bell, P. M. *J. Geophys. Res.: Solid Earth* **1986**, *91* (B5), 4673−4676.
(39) Buscema, M.; Steele, G.; van der Zant, H. J.; Castellanos-Gomez, A. *Nano Res.* **2014**, *7* (4), 1−11.
(40) Kresse, G.; Hafner, J. *Phys. Rev. B* **1993**, *47* (1), 558−561.
(41) Kresse, G.; Joubert, D. *Phys. Rev. B* **1999**, *59* (3), 1758−1775.
(42) Blöchl, P. E. *Phys. Rev. B* **1994**, *50* (24), 17953−17979.
(43) Perdew, J. P.; Burke, K.; Ernzerhof, M. *Phys. Rev. Lett.* **1996**, *77* (18), 3865−3868.
(44) Gonze, X.; Lee, C. *Phys. Rev. B* **1997**, *55* (16), 10355−10368.
(45) Togo, A.; Oba, F.; Tanaka, I. *Phys. Rev. B* **2008**, *78* (13), 134106.

Pressure-Dependent Optical and Vibrational Properties of Monolayer Molybdenum Disulfide

Avinash P. Nayak[1‡], Tribhuwan Pandey[2‡], Damien Voiry[3], Jin Liu[4], Samuel T. Moran[1], Ankit Sharma[1], Cheng Tan[1], Chang-Hsiao Chen[6], Lain-Jong Li[7], Manish Chhowalla[3], Jung-Fu Lin[4,5], Abhishek K. Singh[2], Deji Akinwande[1]**

SUPPLEMENTARY INFORMATION

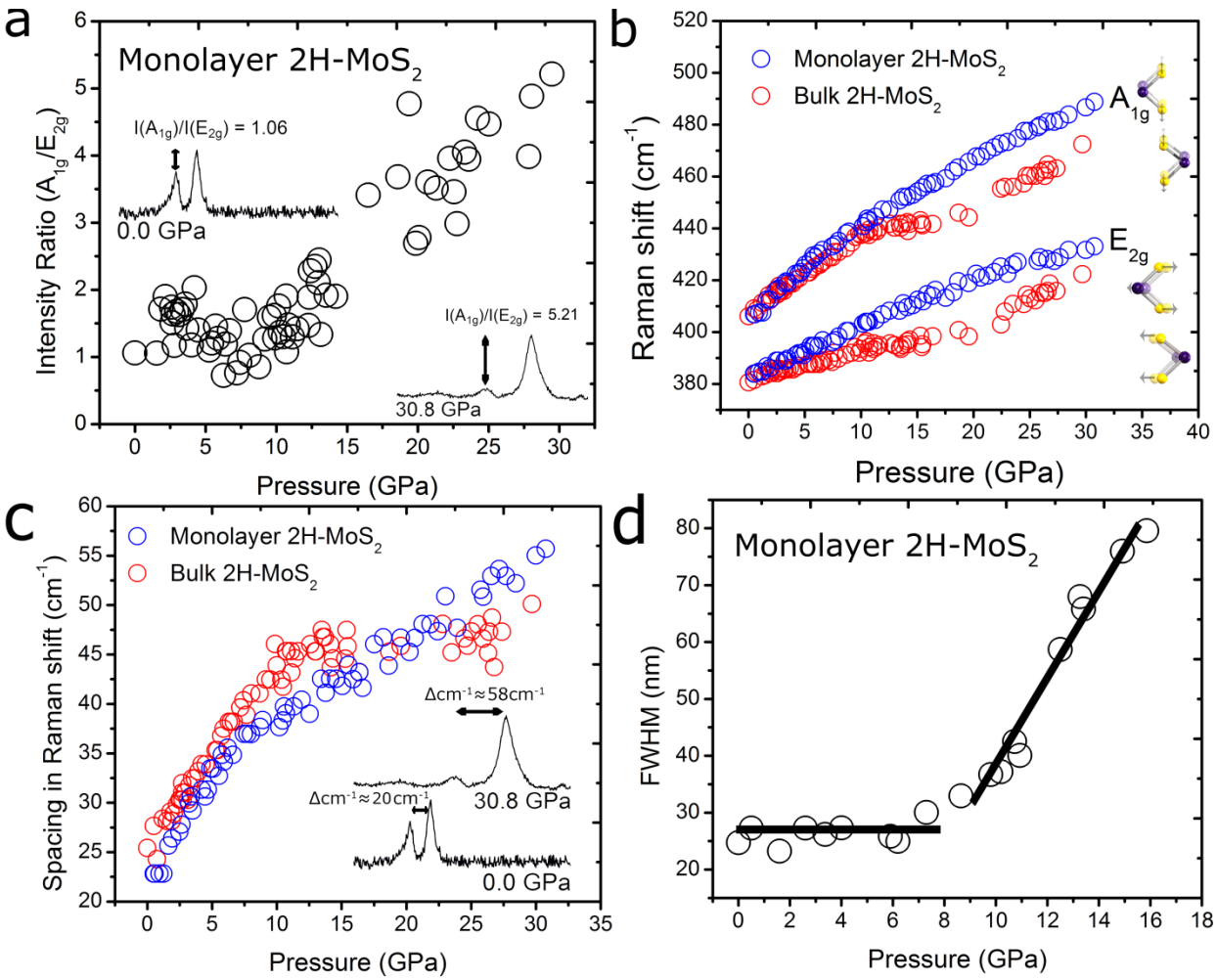

Figure S1. Vibrational and Optical Properties of Bulk and Monolayer 2H-MoS_2 at High Pressures. **(a)** Intensity ratio of the A_{1g} and E_{2g} peaks. The E_{2g} mode is observed to diminish in comparison to the A_{1g}. The insets show the relative intensities of the E_{2g} and A_{1g} peaks at selected pressures. (**b**) Pressure dependence of the Raman frequencies of the A_{1g} and the E_{2g} modes as a function of pressure. The behavior of these vibrational Raman modes in monolayer 2H-MoS_2 at high pressures (blue circles) deviates significantly from that of the bulk counterpart (red circles) due to the absence of interlayer interactions. Inset: representative vibrations involved in A_{1g} and E_{2g} modes. The A_{1g} modes originate from transverse vibrations of S-S atom, however the E_{2g} mode emerges from longitudinal vibrations of Mo and S atoms in opposite directions. (**c**) Raman frequency separation between the A_{1g} and E_{2g} peak as 1) a function of pressure for monolayer and bulk 2H-MoS_2. Inset: representative Raman spectra highlighting the separation at 0 GPa and 30.8 GPa. The in-plane A_{1g} mode becomes more dominant in intensity than the E_{2g} past ~16 GPa for the monolayer 2H-MoS_2. **(d)** PL FWHM with pressure up to 16 GPa. The black lines serves as visual guidelines.

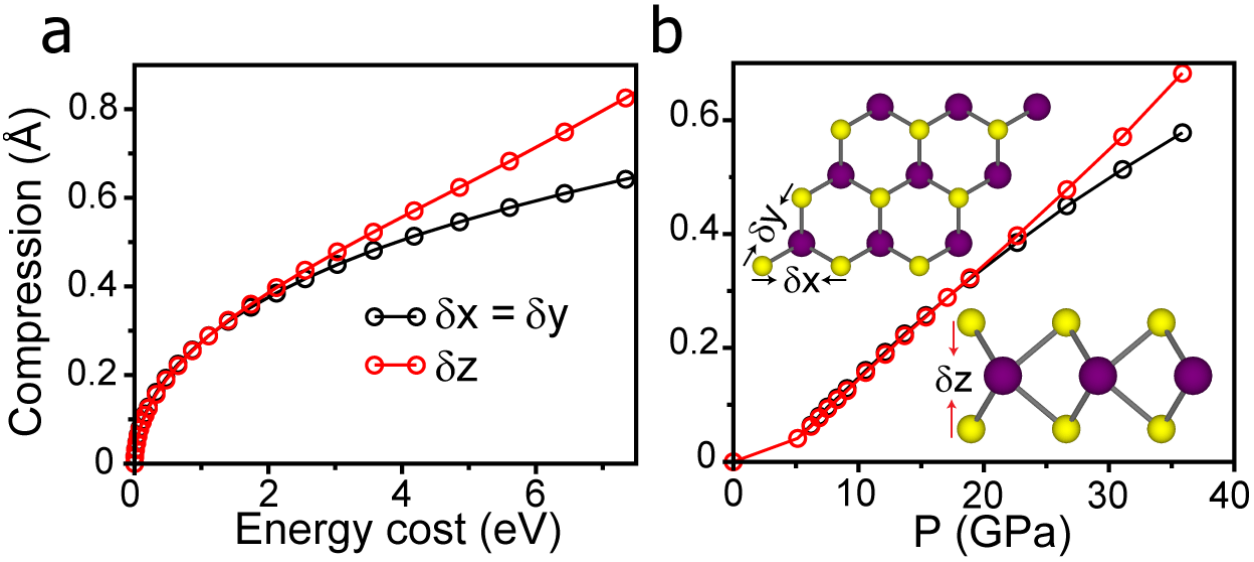

Figure S2. Modeling of hydrostatic pressure on monolayer MoS_2. (a) Compression of atoms plotted with respect to energy required to compress the in-plane (*x*, *y*) and out of plane (*z*) bonds. **(b)** Compression of atoms is plotted with respect to pressure. Till 20 GPa pressure there is equal compression in all the three direction. After 18 GPa. Compression along the *z* direction becomes more favorable. Inset: Schematic representing the compression of atoms in the in-plane direction (upper inset) and out-of-plane directions

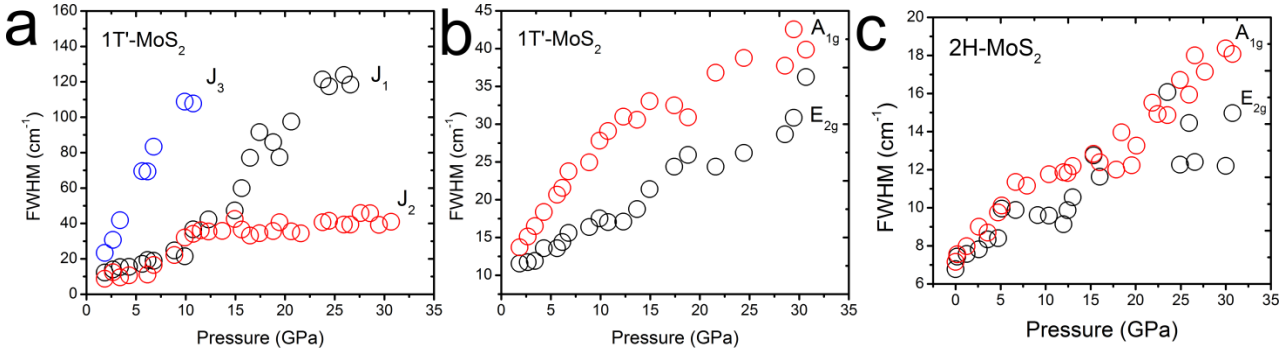

Figure S3. Raman Spectroscopic Results of Restacked 1T'-MoS_2 and monolayer 2H-MoS_2 at High Pressures. (a) FWHM of J_1, J_2 and J_3 Raman modes. The J_3 mode tends to saturate at 10 GPa while J_2 and J_3 increase in FWHM. **(b)** The FWHM of the E_{2g} and A_{1g} increases with pressure. **(c)** The FWHM of the E_{2g} and A_{1g} Raman modes for 2H-MoS_2. The FWHM is notably smaller for the 2H-MoS_2 monolayer than the 1T'-MoS_2 since the J_3 mode merges with the E_{2g} mode.

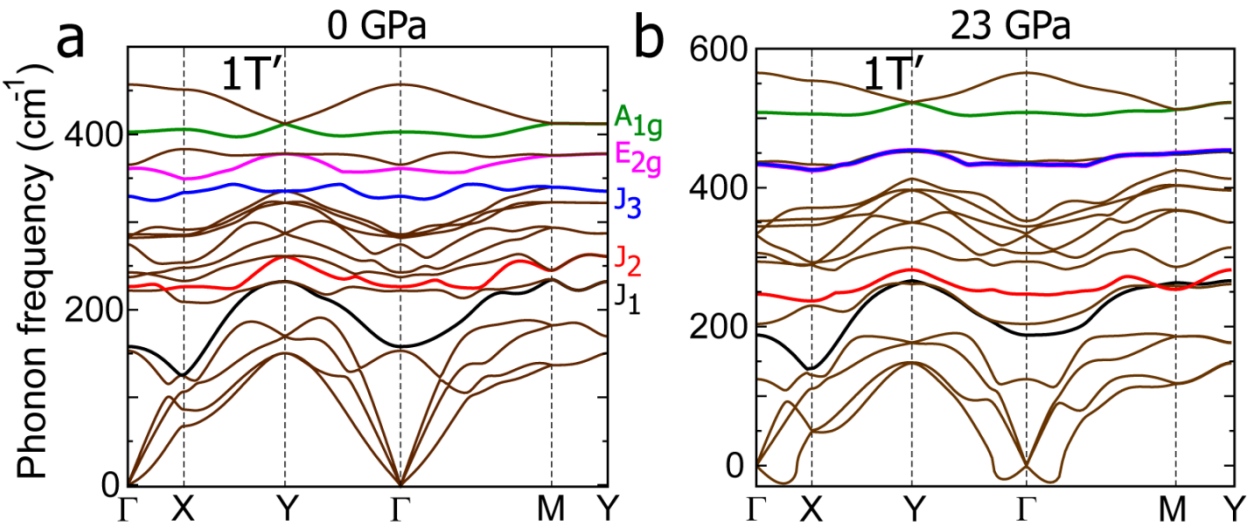

Figure S4. Phonon Dispersions for Monolayer 1T'-MoS_2 at Representative Pressures. The Raman active modes for 1T'-MoS_2 are highlighted with different colors for clarity at **(a)** 0 GPa and **(b)** 23 GPa. The Raman active A_{1g}, E_{2g}, J_1, J_2 and J_3 modes are identified from the dispersion curves at the Γ point. As can be seen in case of 1T'-MoS_2 three new modes J_1, J_2 and J_3 appear, whereas the frequency of the E_{2g} mode decreases significantly compared to bulk MoS_2. The J_3 mode merges with the E_{2g} mode at ~10 GPa.

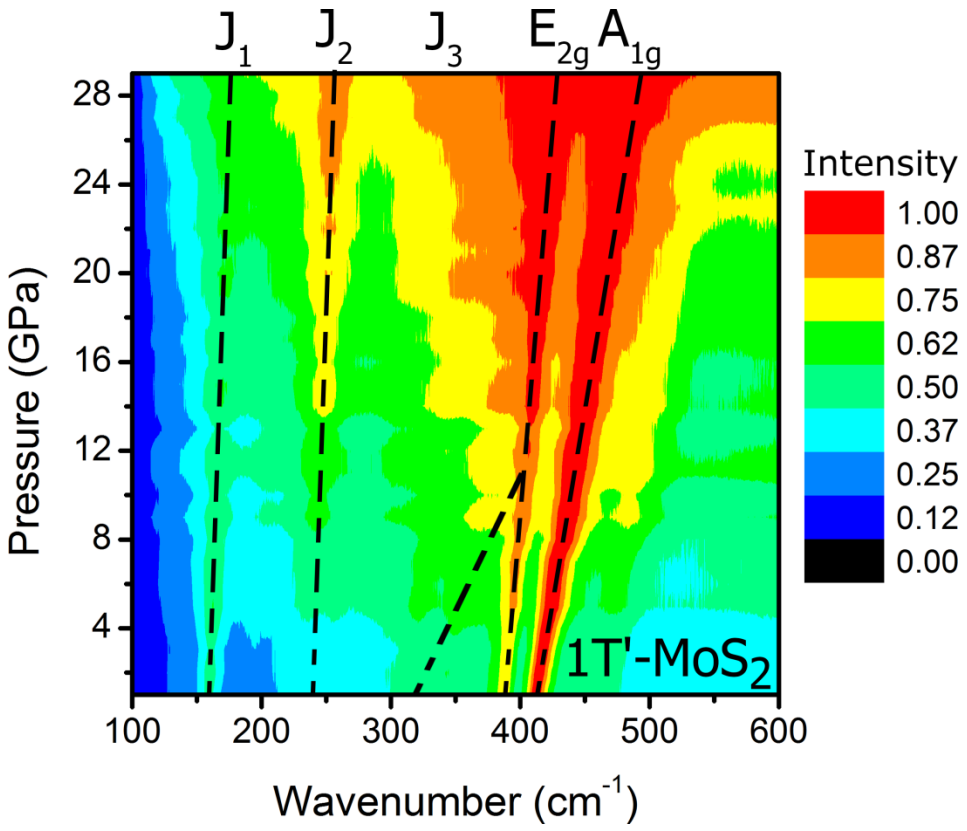

Figure S5. **Raman Intensity Map of 1T'-MoS_2.** The pressure dependent Raman shows the shift and broadening of the 1T'-MoS_2 Raman active modes. The dominant Raman active modes at high pressure are J_2, E_{2g}, and A_{1g}.

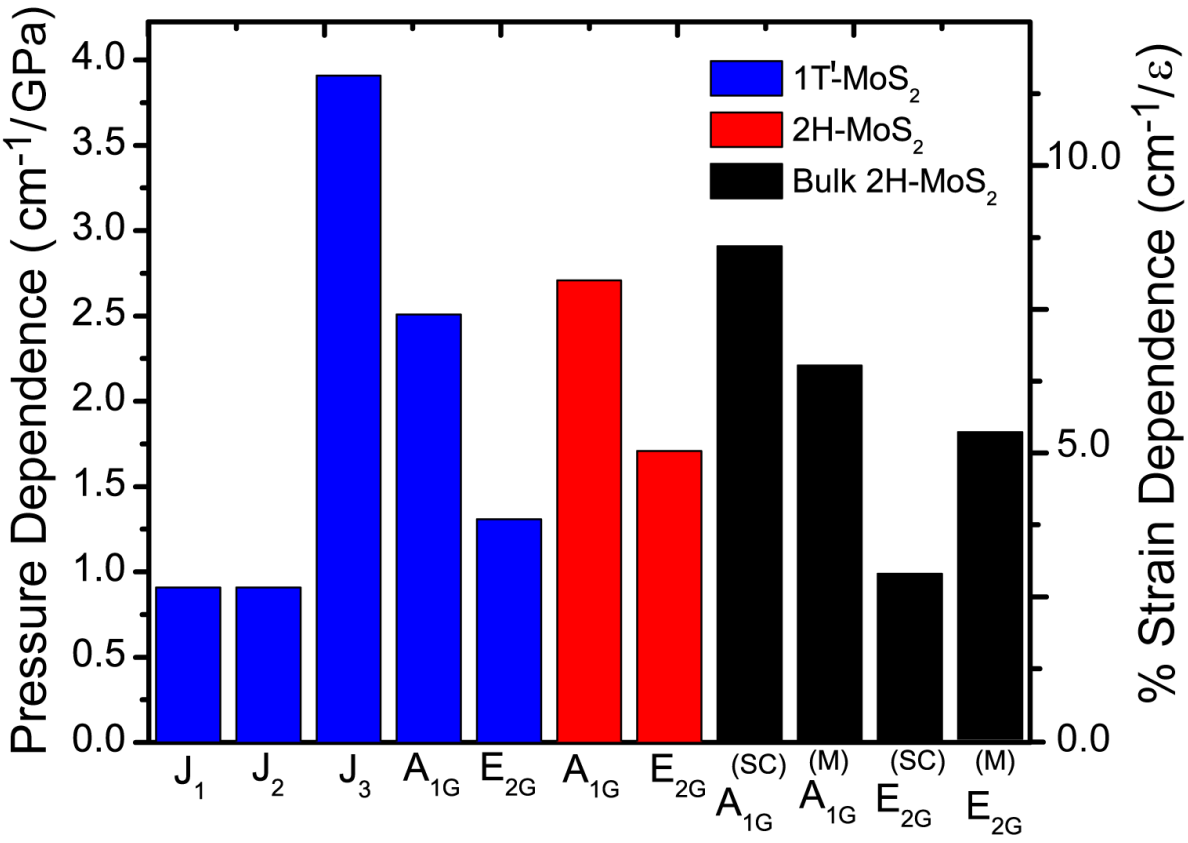

Figure S6. Raman Shift with Pressure. The pressure dependence of the Raman modes for the monolayer 2H and 1T'-MoS_2 polytypes compared to the bulk 2H-MoS_2 analog in their semiconducting (SC) and metallic (M) regime.

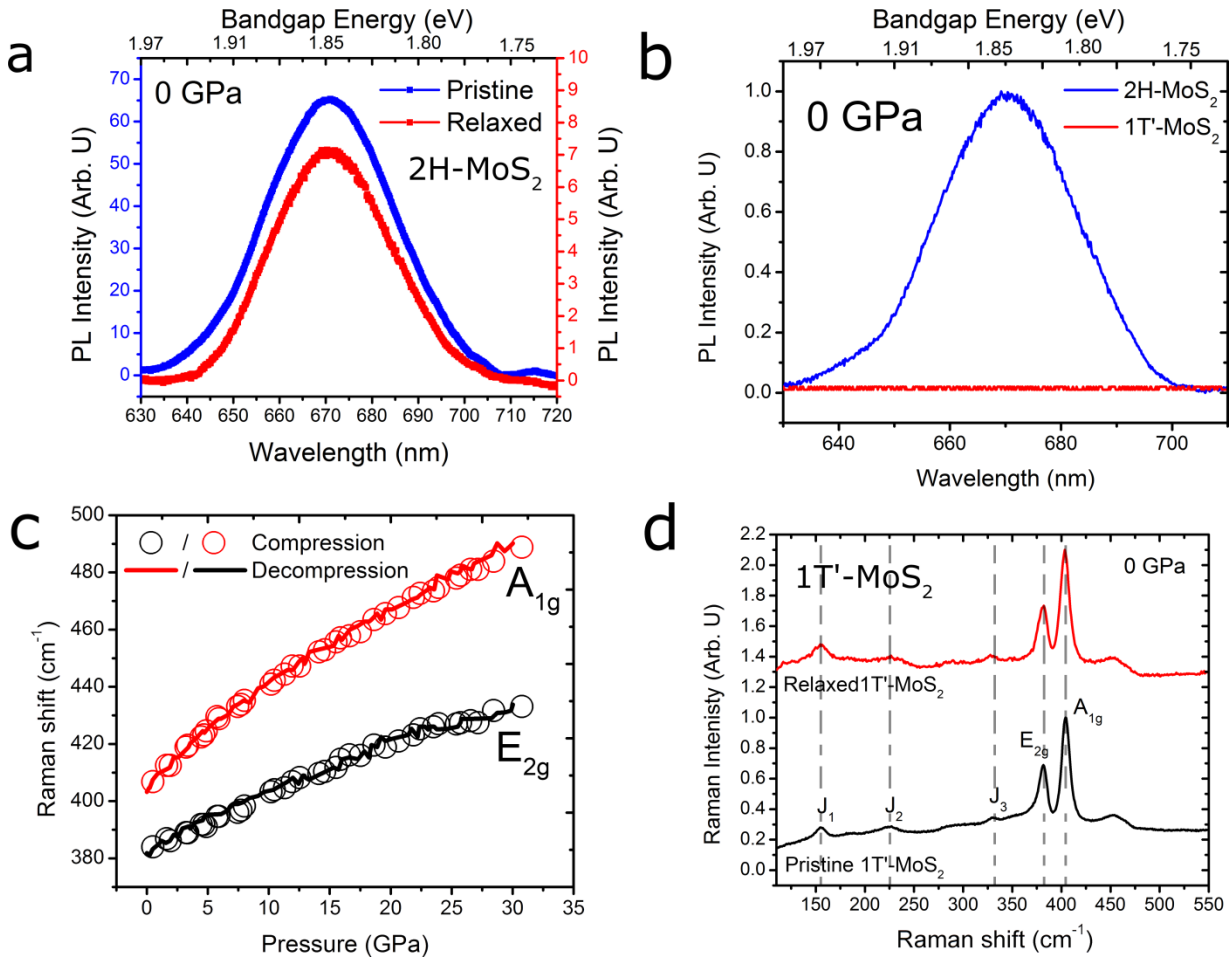

Figure S7. Reversible Pressure Effects on Monolayer MoS_2. (a) PL from monolayer MoS_2 before and after hydrostatic pressure of 30 GPa is applied across the monolayer 2H-MoS_2. **(b)** The PL for the 1T'-MoS_2 and 2H-MoS_2 at 0 GPa. The 1T'-MoS_2 does not show PL behavior. **(c)** Upon decompression, the Raman active A_{1g} and E_{2g} modes compare well with the Raman spectra with increasing pressure, suggesting that the pressure effects are reversible. **(d)** Pristine and relaxed 1T'-MoS_2 show the J_1, J_2, and J_3 active modes, indicating that the pressure effects are reversible.

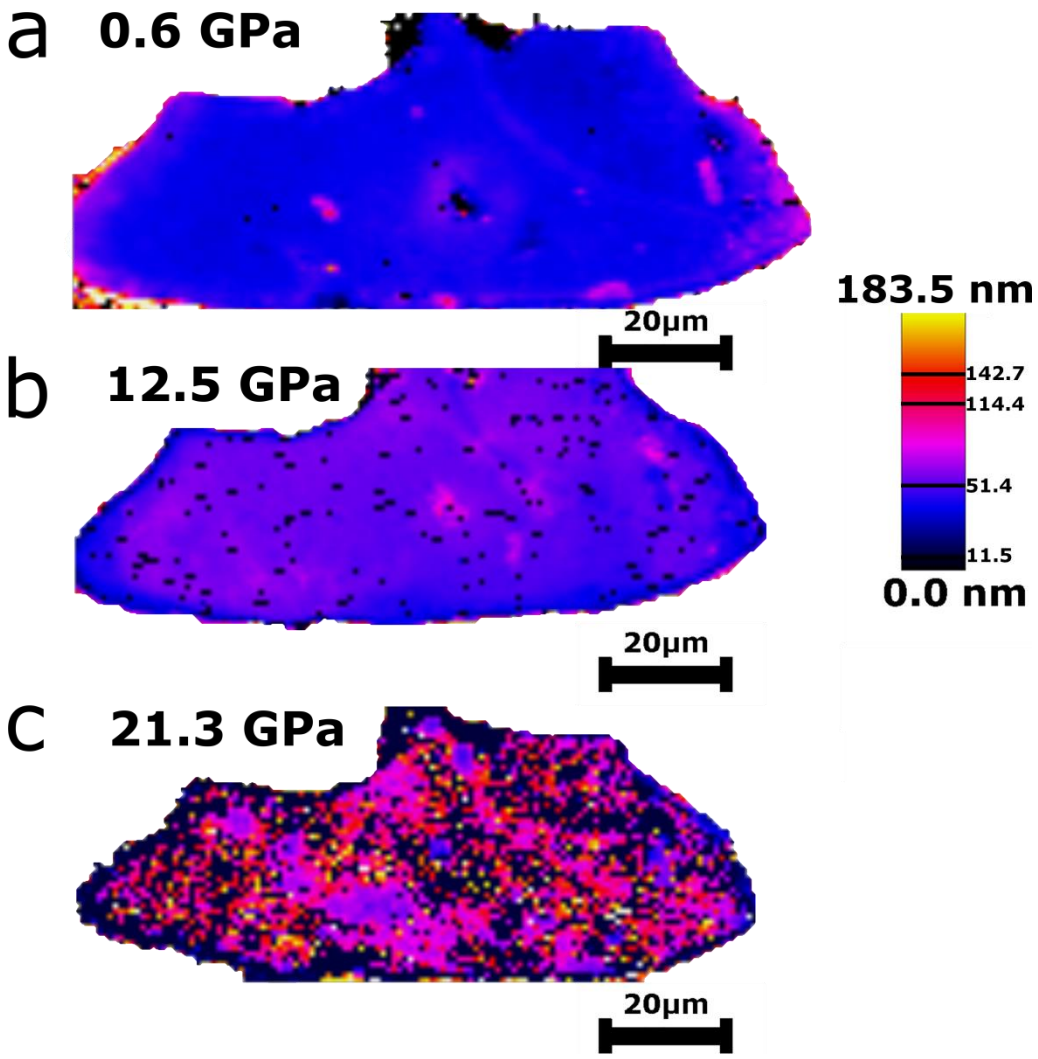

Figure S8. FWHM of the PL Spectra from Monolayer MoS_2. (a) The FWHM map showing an increase with hydrostatic pressure at **(a)** 0.6 GPa **(b)** 12.5 GPa and **(c)** 21.3 GPa the diminishing of the PL peak that suggest the PL at high pressures is unresolvable past 16 GPa at room temperature. The black dots represent where the peaks are diminished into the background noise.

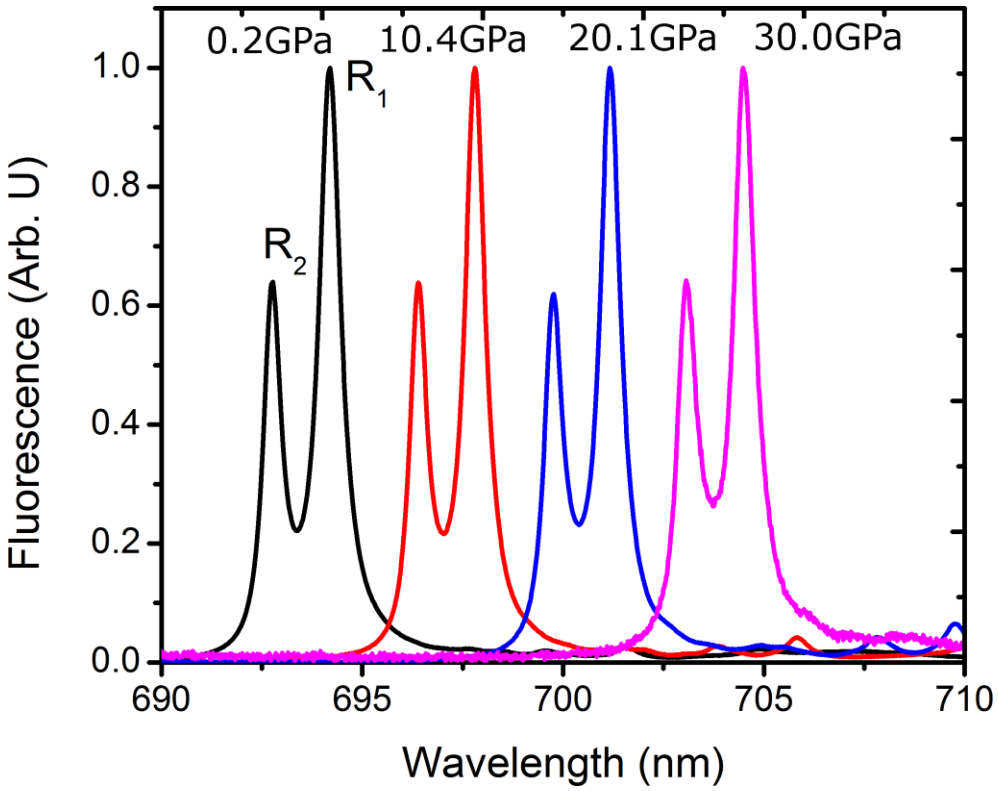

Figure S9. Fluorescence Spectra Shift in Ruby. The R_2 and R_1 ruby luminescence peaks are used to measure the pressure shift. The evolution of the PL spectra from ruby is used as a calibrant to measure the pressure experienced by the sample.

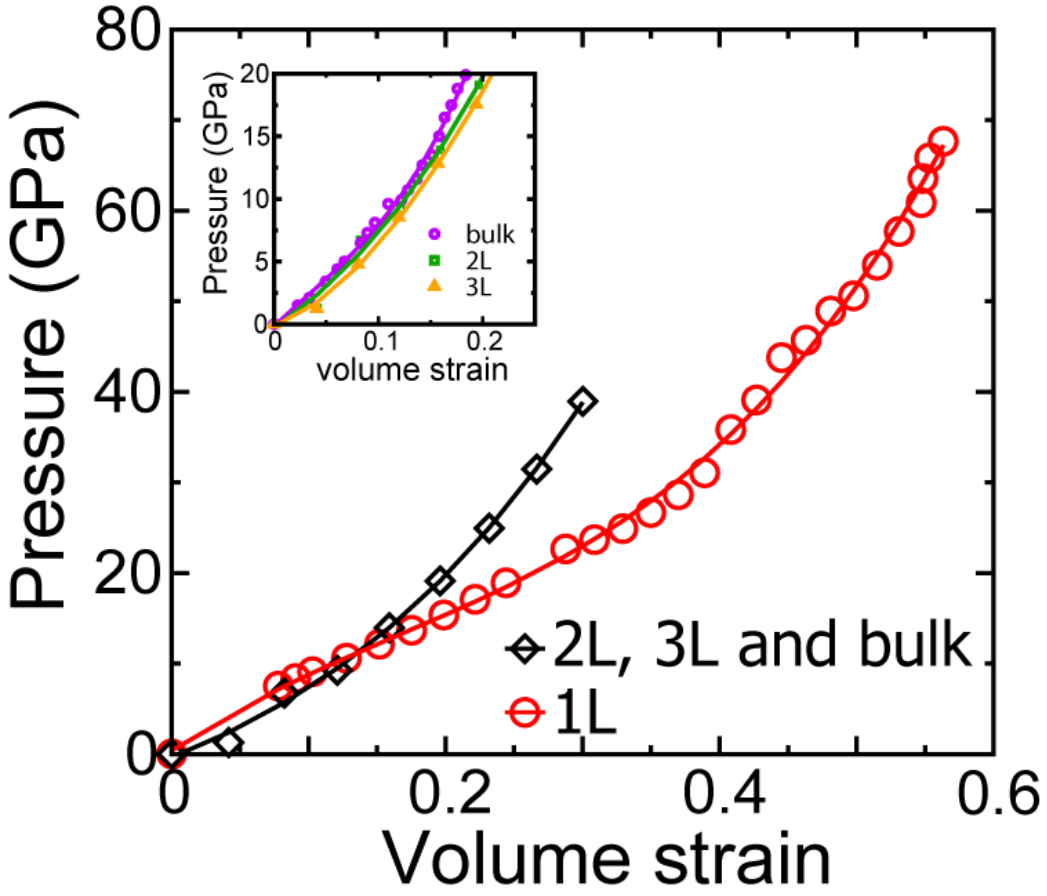

Figure S10. Relation between Volume Strain and Pressure for 2H-MoS_2 Family. 2L, 3L and Bulk follow the same trend and the data can be fitted to a third order polynomial as $P = -0.36 + 59.81\varepsilon + 137.96\varepsilon^2 + 325.93\varepsilon^3$. However 1L depicts a completely different behavior, the polynomial fit of 1L data can be given as $P = 0.39 + 101.24\varepsilon - 220.72\varepsilon^2 + 446.7\varepsilon^3$. These different behaviors arise due to absence of interlayer interaction for monolayer MoS_2. Inset: 2L, 3L and bulk have almost same dependence between volume strain and pressure.

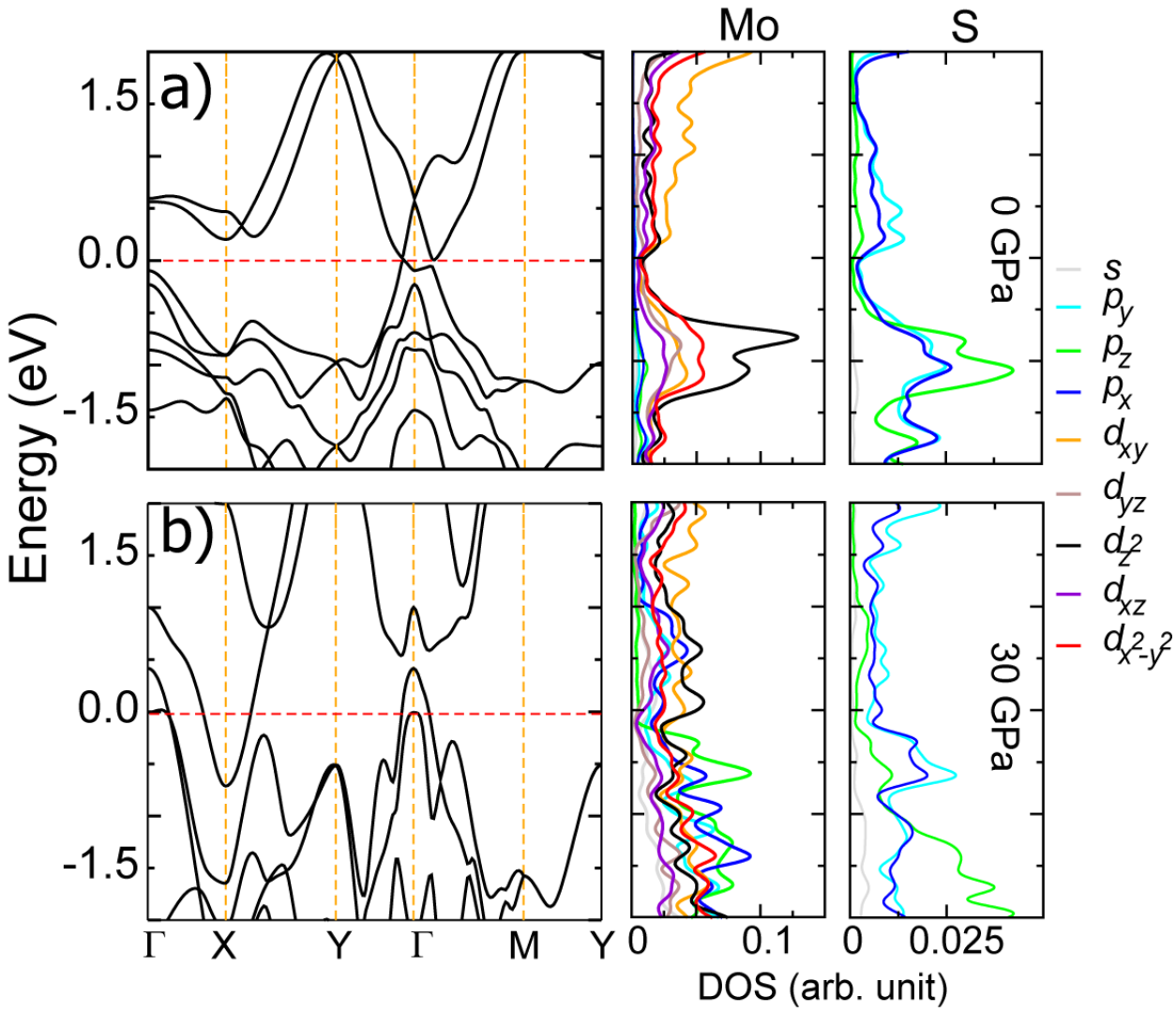

Figure S11. Band Structure and Density of States for the 1T'-MoS_2 Monolayer. (a) At 0 GPa pressure and **(b)** 30 GPa. The monolayer 1T'-MoS_2 is metallic and becomes more metallic under hydrostatic pressure. Upon application of hydrostatic pressure the hybridization between Mo *d*-orbitals (mainly d_{z^2}, d_{xy} and $d_{x^2-y^2}$) and S *p*-orbitals increases, there is an increase in the overlap between conduction and valence bands, increasing the extent of metallization.

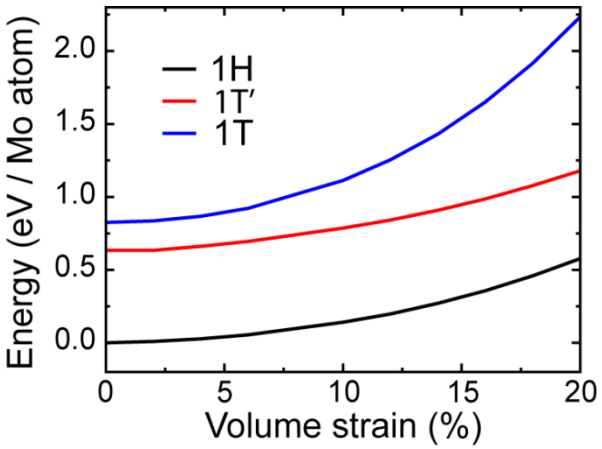

Figure S12. Stability of Different MoS_2 Monolayer Polytypes with Respect to the 2H-MoS_2 Monolayer as a Function of Volume Strain. Monolayer 2H-MoS_2 (i.e. 1H-MoS_2) is the most stable phase at ambient conditions and remains energetically favorable even under high strains. The absence of cross over between the various energy plots indicates the absence of phase transformation between 2H and monolayer 1T'-MoS_2 which is in agreement with our Raman spectra.

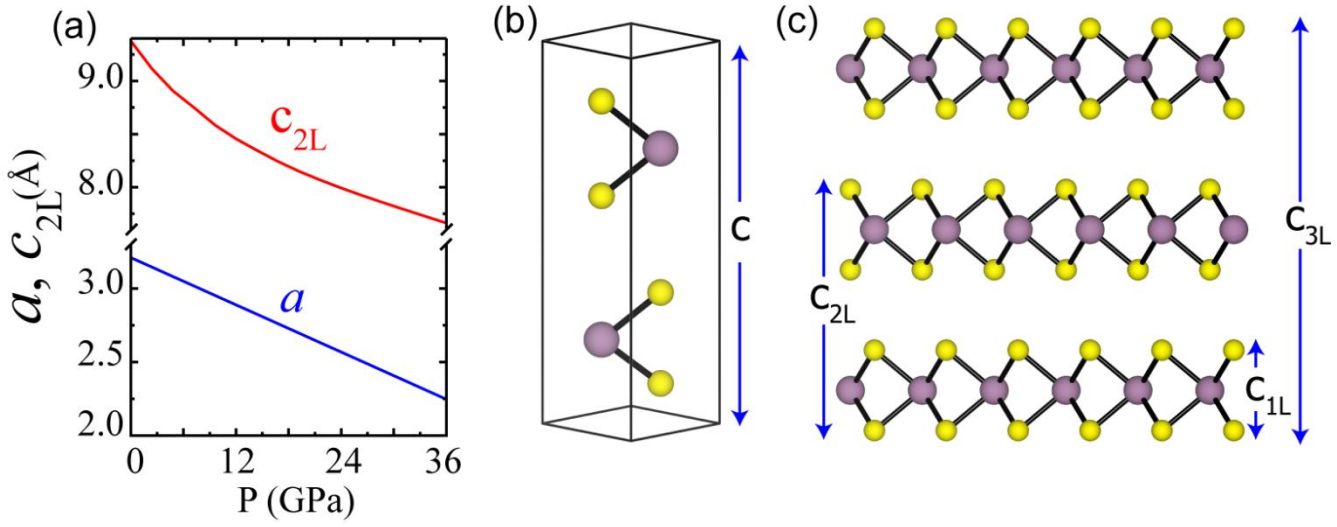

Figure S13. **Compression of the in-plane and out-of plane axis. (a)** Variation in slab thickness (c_{2L}) and in-plane lattice parameter *a* under hydrostatic pressure**.** Illustration of slab thickness for **(b)** bulk and **(c)** 1L, 2L, and 3L MoS_2.